Contents lists available at ScienceDirect

Precambrian Research

Temperature and timing of ductile deformation of the Longquanguan shear zone, Trans-North China Orogen

Jia-Hui Liu [a], Yi-Chao Chen [a,*], Zhen M.G. Li [a], Qian W.L. Zhang [a], Ting-Guang Lan [b], Qing Zhang [c], Chun-Ming Wu [a]

[a] College of Earth and Planetary Sciences, University of Chinese Academy of Sciences, P.O. Box 4588, Beijing 100049, China
[b] State Key Laboratory of Ore Deposit Geochemistry, Institute of Geochemistry, Chinese Academy of Sciences, Guiyang 550081, China
[c] Institute of Geomechanics, Chinese Academy of Geological Sciences, Beijing 100081, China

ARTICLE INFO

ABSTRACT

Determination of temperature conditions and timing of ductile shearing is important in understanding the deformation mechanisms and tectonic evolution. The Longquanguan shear zone locates in the middle section of the Trans-North China Orogen, extending ~ 100 km long in NNE-SSW direction and exposing abundant granitic and granodioritic mylonites, characterized by well-developed NW-dipping mylonitic foliation and penetrative NW-plunging mineral stretching lineation. The mylonite exhibits regionally heterogeneous mechanisms of dynamic recrystallization, dominated by subgrain rotation. Ti-in-quartz (TitaniQ) geothermometer was applied to assess the deformational temperature along five profiles across this shear zone. In the northern part of this shear zone, quartz ribbons of the three narrower profiles display relatively homogeneous Ti content and record similar temperatures of 474–505 °C, 500–539 °C, and 492–521 °C, respectively. In the southern part, quartz ribbons of the two wider profiles show eastward increasing Ti content and record temperature increasing from 440 to 557 °C, and from 461 to 553 °C, respectively. A temperature gradient is estimated to be 20–25 °C/km, which possibly relates to the geothermal gradient between the hanging wall and the footwall. The shear zone, along with the temperature gradient narrows out to the north, possibly resulted from differential erosion/denudation. The hornblende and mica $^{40}Ar/^{39}Ar$ age data indicate that the ductile deformation occurred at ~ 1.85–1.80 Ga, followed by quick cooling occurred at 1.83–1.78 Ga. Therefore, the Longquanguan shear zone records ductile shear deformation, which possibly occurred during the collision between the Western and Eastern Blocks of the NCC in the Late Paleoproterozoic.

1. Introduction

Shear zone occurs in the mid-lower crust and even the upper mantle (e.g., Vauchez et al., 2012), typically composed of simple shear and pure shear components (e.g., Fossen and Cavalcante, 2017). Shear zone is the deeper counterpart of the upper fault zones in thrust, extensional, and strike-slip settings, which contains abundant information to link the small-scale structures to larger-scale tectonics (Cottle et al., 2015; Fossen, 2010; Fossen and Cavalcante, 2017; Godin et al., 2006). The microfabrics of the shear zone can be affected by many factors such as mineralogy, grain size, temperature, pressure, fluids, and strain rate, in which temperature is generally considered to be the most important factor (e.g., Cavalcante et al., 2018; Passchier and Trouw, 2005; Fossen and Cavalcante, 2017). Therefore, estimation of thermal conditions is

critical to uncover the deformation mechanism. More importantly, assessment of deformational temperature can help us understand the deformational depth, deformational timing, exhumation history, and further the tectonic evolution (e.g., Bestmann and Pennacchioni, 2015; Cross et al., 2015; Wang et al., 2005; Xia and Platt, 2019).

However, quantification of deformation temperature is not easy. With the operation of a series of experiments on deformation mechanism and rheology of quartz (e.g., Hirth and Tullis, 1992; Tullis, 1977; Tullis et al., 1973), the slip systems in quartz were established and they usually indicate qualitative temperature ranges. For example, generally, with the increase of thermal conditions, the activation of quartz slip systems is from basal <a>, rhomb <a>, prism <a>, to prism <c> (Passchier and Trouw, 2005). Stipp et al. (2002) reviewed systematic temperature ranges of three dynamic recrystallization mechanisms in naturally
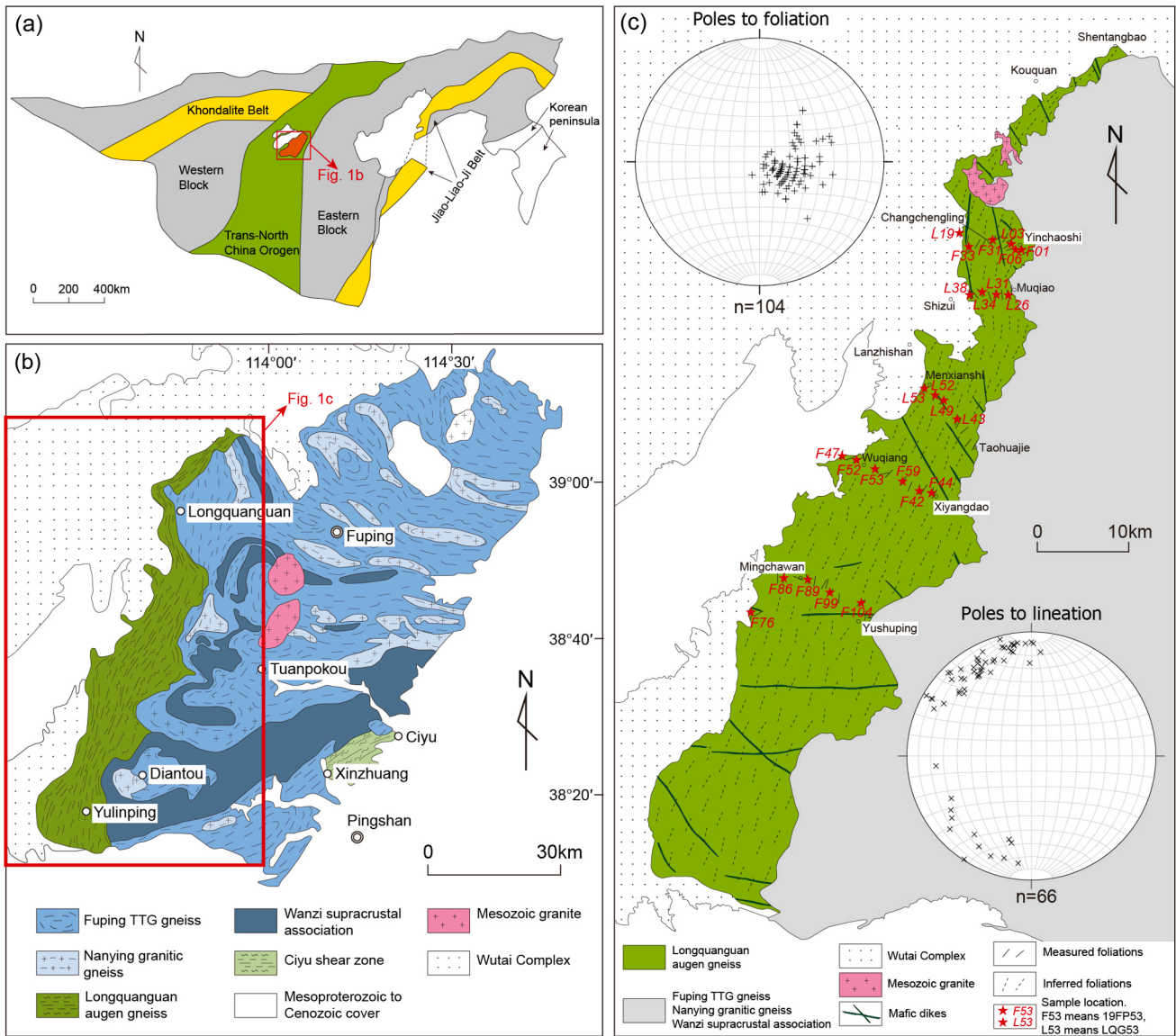
Fig. 1. (a) Tectonic subdivision of the North China Craton (after Zhao et al., 2005). (b) Geological map of the Fuping Complex (after Zhao et al., 2000). (c) Geological sketch of the Longquanguan shear zone (after 1:200000 Geological maps of Pingxingguan and Yuxian). The foliation and lineation projections were plotted as the lower hemisphere, equal area.

deformed quartz, i.e., bulging recrystallization (~280–400 °C), subgrain rotation recrystallization (~400–500 °C), and grain boundary migration recrystallization (~500–700 °C), serving as a semi-quantitative tool to assess deformation temperatures. Kruhl (1998) developed the quartz c-axis fabric opening-angle thermometer based on the natural data, nevertheless, this thermometer is also sensitive to strain rate and water weakening (Law, 2014). Moreover, some researchers have applied traditional petrology-based geothermobarometers to constrain the deformation *P-T* conditions (e.g., Cao et al., 2007; Leloup and Kienast, 1993; Liang et al., 2015; Zhang et al., 2018), which also have some limitations: (1) it needs to find appropriate mineral assemblages for applying suitable mineralogical geothermobarometers (Cavalcante et al., 2018); and (2) it needs to identify dynamic deformational mineral assemblages, discriminated from inherited magmatic or metamorphic mineral assemblages (Zhang et al., 2018). In the last decade, the accurate and easily used Ti-in-quartz (TitaniQ) geothermometer becomes a vital method to evaluate the deformation temperature. Wark and Watson (2006) originally established the TitaniQ geothermometer based on the relationship between titanium concentration in quartz and crystallization temperatures. Later, Thomas et al. (2010) as well as Huang and

Audétat (2012) found that the substitution of Ti^{4+} for Si^{4+} in quartz is also pressure-sensitive, thus they refined this geothermometer based on experimental data of various *P-T* conditions. Compared with other geothermometers, the TitaniQ geothermometer is claimed superiority in estimating deformation temperature (Cavalcante et al., 2018; Kohn and Northrup, 2010): (1) quartz occupies high abundance in most natural mylonite; (2) quartz accommodates primary strain in the crust; and (3) typical temperatures of mylonitization (<500 °C) cannot be readily estimated by traditional cation-exchange thermometers. Such advantages make the TitaniQ geothermometer being widely applied to constrain the thermal conditions of naturally deformed rocks, ranging from ~350 °C to ~800 °C (Ashley et al., 2013; Bestmann and Pennacchioni, 2015; Cavalcante et al., 2014; 2018; 2011;; Cross et al., 2015; Grujic et al., 2009; Haertel et al., 2013; Hughes et al., 2019; Kohn and Northrup, 2010; Pennacchioni et al., 2010; Xia and Platt, 2019).

The Paleoproterozoic Trans-North China Orogen (TNCO, Fig. 1a; Zhao et al., 1998; 2001; 2005), or the Central Orogenic Belt (COB, Kusky and Li, 2003; Kusky et al., 2016; Wang et al., 2015; 2019a), is an important tectonic unit which was produced in the amalgamation of the Eastern and Western Blocks and the final formation of the coherent

Table 1
Main mineral modes (vol.%) of representative mylonite samples.

Profile	Location	Sample	Lithology	Hbl	Bt	Mus	Ser	Chl	Fsp	Qz	Others
Changchengling-Yinchaoshi	113°44′7′′E, 38°55′57′′N	LQG19	Mylonitic schist			5		20	40	30	Rt, Zr, Mag
	113°44′50′′E, 38°54′59′′N	19FP33	Granitic mylonite	5	30				30	30	Ttn, Ilm, Zrn
	113°46′39′′E, 38°55′31′′N	19FP31	Granodioritic mylonite	20	15			5	30	25	Rt, Ttn, Py
	113°47′41′′E, 38°55′14′′N	LQG03	Granodioritic mylonite	20	15				35	25	Ttn, Mag, Zrn
	113°48′23′′E, 38°54′55′′N	19FP06	Granitic mylonite		20				40	35	Rt, Ttn, Ilm, Zrn, Mag
	113°48′47′′E, 38°54′56′′N	19FP01	Granitic mylonite		5				50	40	Rt, Zrn, Mnz, Mag
Shizui-Muqiao	113°44′51′′E, 38°52′13′′N	LQG38	Granitic mylonite		30				35	30	Zrn, Mag
	113°45′48′′E, 38°52′26′′N	LQG34	Granitic mylonite		20				45	30	Zrn, Mag
	113°47′41′′E, 38°55′14′′N	LQG31	Dioritic mylonite	40	10				30	15	Ttn, Zrn, Mag
	113°47′49′′E, 38°52′14′′N	LQG26	Granodioritic mylonite	25	15				35	20	Ttn, Py, Mag
Menxianshi-Taohuajie	113°41′30′E, 38°46′43′′N	LQG53	Mylonitic amphibolite	80					8	8	Ttn, Mag, Zrn
	113°42′15′E, 38°46′18′′N	LQG52	Granitic mylonite		20	5			40	30	Ilm, Mag, Zrn
	113°42′55′E, 38°45′58′′N	LQG49	Granitic mylonite		30	5			30	30	Hem, Zrn
	113°43′57′E, 38°44′59′′N	LQG43	Granodioritic mylonite	20	15				35	25	Ttn, Mag, Zrn
Wuqiang-Xiyangdao	113°35′14′E, 38°42′41′′N	19FP47	Granitic mylonite		15	20			30	30	Zrn, Mag, Ilm
	113°36′24′E, 38°42′24′′N	19FP52	Mylonitic schist		30		10		25	30	Rt, Ttn, Mag, Ep
	113°37′48′′E, 38°41′54′′N	19FP53	Mylonitic schist		20			40	5	30	Rt, Ttn, Ilm, Py, Tur
	113°39′52′′E, 38°41′10′′N	19FP59	Mylonitic sandstone		10				15	70	Zrn, Mag
	113°41′06′′E, 38°40′34′′N	19FP42	Granodioritic mylonite	20	5				50	20	Rt, Ttn, Mag
	113°42′01′′E, 38°40′28′′N	19FP44	Granitic mylonite		15				40	40	Ilm, Mag
Mingchawan-Yushuping	113°28′28′′E, 38°33′18′′N	19FP76	Quartzofeldsphatic mylonite			30		5	25	35	Hem, Mag, Zrn
	113°30′54′′E, 38°35′32′′N	19FP86	Granitic mylonite		15				40	40	Rt, Ttn, Ilm, Zrn, Mag
	113°32′37′′E, 38°35′23′′N	19FP89	Granitic mylonite		15				50	30	Ilm, Ttn, Mag, Zrn
	113°34′38′′E, 38°34′30′′N	19FP99	Granitic mylonite		15				40	40	Ilm, Mag, Zrn
	113°37′10′′E, 38°33′19′′N	19FP104	Granitic mylonite		25			3	40	30	Mag, Ilm, Zrn, Mnz, Apt

Mineral abbreviations are after Whitney and Evans (2010).

basement of the North China Craton (NCC) in the Paleoproterozoic. Shear zones of various scales outcrop in the TNCO (e.g., He et al., 2020; Qian et al., 2019; Zhao et al., 2019). The Longquanguan shear zone, located in the middle of the TNCO (Fig. 1a), was generally regarded as a tectonic boundary separating the Wutai and Fuping Complexes (Fig. 1b–c; e.g., Zhao et al., 2000; Li et al., 2010). This shear zone extends ~100 km long in NNE-SSW direction, with preferred foliation dipping to NW-NWW, and preferred mineral stretching lineation plunging to NW-NNW. Based on the S-C fabrics, asymmetric augen structures, asymmetric fold, and the bookshelf structures, some researchers (Li and Qian, 1991; Pei et al., 2001; Sun et al., 2004; Zhao et al., 2006) proposed one to two phases of deformation, which is dominated by the top-to-southeast shearing under thrusting tectonics, overprinted by a later phase of top-to-southeast or top-to-northwest shearing. On the contrary, other researchers (e.g., Zhao et al., 2019) proposed a single phase extension with a top-to-northwest sense of shear. Using traditional geothermobarometry, quartz decrepitation, and oxygen isotope geothermobarometry, the deformation *P-T* conditions of the Longquanguan shear zone were estimated to be 290–575 °C/3.0–8.6 kbar (Li and Qian, 1991) or 350–486 °C (Xu et al., 1995). The deformation age was dated to be 1952–1914 Ma by biotite/hornblende $^{40}Ar/^{39}Ar$ dating method for the mylonite (Xu et al., 1995) or 1877–1782 Ma by EPMA U-Th-Pb dating on monazite from the *syn*-deformational granite (Zhao et al., 2006). However, both the *P-T*

conditions and ages of ductile deformation were focused on limited locations (e.g., Changchengling-Yinchaoshi profile, Xu et al., 1995). Considering the size (~100 km long and ~15 km wide) of the Longquanguan shear zone, the deformation *P-T* conditions are more likely complex or heterogeneous along and across the regional-scale shear zone. Therefore, we investigated five geologic profiles from the north to the south transecting this shear zone, and applying the newly calibrated, accurate Ti-in-quartz (TitaniQ) geothermometer to reevaluate the temperature conditions of ductile shear. Furthermore, we applied $^{40}Ar/^{39}Ar$ incremental heating method to infer the timing on deformation for this shear zone to refine our understanding on the tectonic evolution of this shear zone.

2. Geological setting

The North China Craton (NCC) is the largest and oldest craton in China, which was possibly formed during the assembly of several microblocks, albeit the tectonic pattern and timing remain controversial (e.g., Zhao et al., 1998; 2001; 2005;; Kusky and Li, 2003; Kusky et al., 2016). Based on one popular tectonic model of Zhao et al. (1998); (2001; 2005;)), the NCC was formed through aggregation of the Western and Eastern Blocks along the nearly NS-striking TNCO at ~1.85 Ga, which was involved in the polymerization of Paleoproterozoic Nuna/Columbia supercontinent (e.g., Zhao et al., 2002a; Rogers and Santosh, 2002; Wan
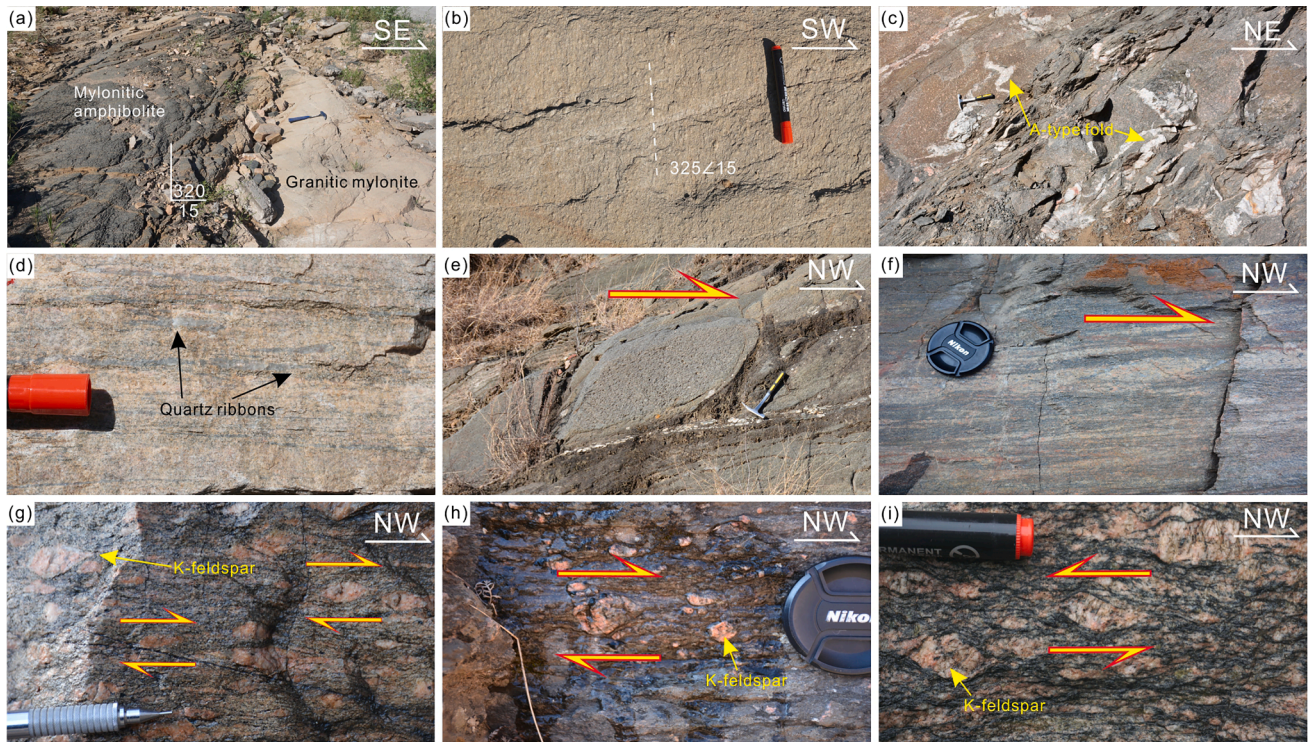
Fig. 2. Field shots of ductilely deformed mylonites from the Longquanguan shear zone. (a–b) Mylonitic amphibolite is interbedded with granitic mylonite, both of them show identical foliation and lineation. Fig. 2(b) is a close view of (a). (c) A-type fold with a hinge plunging to 320°. (d) Quartz ribbons consist of elongated quartz. (e) Lenses-shaped deformed layers form the S-C fabrics, indicating a shear sense of top-to-northwest. (f) Sheared veins form the S-C fabrics, suggesting a shear sense of top-to-northwest. (g–i) Feldspar grains deform plastically, and turned into asymmetric porphyroclasts. Fig. 2g–h indicates a shear sense of top-to-northwest, whereas Fig. 2i suggests top-to-southeast.

et al., 2015; 2020).

The Fuping Complex is located in the middle of the TNCO and adjoins the Hengshan and Wutai Complexes. The Fuping Complex is composed of four lithological-tectonic units, i.e., the Fuping TTG gneiss, the Wanzi supracrustal association, the Nanying gneissic granite, and the Longquanguan shear zone. The Fuping TTG gneiss records crystallization ages mostly of 2.52–2.48 Ga (Guan et al., 2002; Han et al., 2012; Liu et al., 2002; Zhao et al., 2002b), and usually includes granulite and amphibolite enclaves. The Wanzi supracrustal association is dominated by amphibolite facies rocks, including gneiss, pelitic schist, calc-silicate rocks, marble, and amphibolite. The ages of detrital zircons of the supracrustal rocks are dated to be 2.5–2.1 Ga (Guan et al., 2002; Ren et al., 2013; Xia et al., 2006; Zhao et al., 2002b). The Nanying gneissic granite consists of weakly deformed monzonitic granite, sillimanite granite, and K-feldspar granite, with the protolith possibly emplaced around 2.10–2.02 Ga (Guan et al., 2002; Zhao et al., 2002b). The Longquanguan shear zone is mainly composed of granitic and granodioritic mylonite. TIMS (Xu et al., 1995) and LA-ICP-MS (Wang et al., 2019b) U-Pb dating of zircons from the augen mylonite yielded ages of ~2.50 Ga and ~2.55 Ga, respectively, which were interpreted as crystallization age of the granite/granodiorite protolith. $^{40}Ar/^{39}Ar$ dating of biotite and Rb-Sr isochron dating of whole-rock from augen mylonite (Xu et al., 1995), as well as EPMA U-Th-Pb dating of monazite from *syn*-deformational granites (Zhao et al., 2006), yielded ages of 1952–1914 Ma and 1877–1782 Ma, respectively, which were interpreted as the deformation age. The whole Fuping Complex records extensive amphibolite-granulite facies metamorphism during 1.89–1.80 Ga (Guan et al., 2002; Liu et al., 2002; 2019; 2021a; 2021b;; Meng et al., 2017; Qian et al., 2018; Xia et al., 2006; Zhao et al., 2002b), then 1.78–1.75 Ga unmetamorphosed mafic dike swarms emplace in the Fuping and the whole NCC, possibly indicating an extensional tectonic setting (e.g., Peng et al., 2005).

3. Field occurrence and sample description

Twenty-five mylonite samples were collected from five geologic profiles in the Longquanguan shear zone from north to south, i.e., the Changchengling-Yinchaoshi, Shizui-Muqiao, Menxianshi-Taohuajie, Wuqiang-Xiyangdao, and Mingchawan-Yushuping sections (Fig. 1c; Table 1). These include granitic mylonite (samples 19FP33, 19FP06, 19FP01, LQG38, LQG34, LQG52, LQG49, 19FP47, 19FP44, 19FP86, 19FP89, 19FP99, and 19FP104), granodioritic mylonite (19FP31, LQG03, LQG26, LQG43, and 19FP42), dioritic mylonite (LQG31), quartzofeldspathic mylonite (19FP76), mylonitic amphibolite (LQG53), mylonitic schist (LQG19, 19FP52, 19FP53), and mylonitic sandstone (19FP59). In the field, these mylonites exhibit moderately to intensively ductile fabrics, with a preferred foliation dipping to NW-NWW, and a preferred mineral stretching lineation plunging to NW-NNW (Fig. 1c). The penetrative mineral stretching lineation (Fig. 2a–b), a-type fold (Fig. 2c), sheared quartz ribbons, layers and veins (Fig. 2d–f), and ductilely deformed K-feldspar grains (Fig. 2g–i) indicate extensive ductile deformation. Lenses-shaped deformed layers (Fig. 2e), deformed veins (Fig. 2f), and plastically deformed feldspar grains (Fig. 2g–i, note the recrystallized tails of feldspar) indicate a dominant top-to-northwest shear sense. Feldspar grains deform plastically (Fig. 2g–i), which indicates a high-temperature deformation (e.g., Jessell, 1987; Passchier and Trouw, 2005; Stipp et al., 2002; Tullis and Yund, 1987).

On microscopic scales, these mylonites show heterogeneous deformation features. In sample 19FP76 from the west part of the shear zone, fine-grained quartz crystals were observed rimming the large quartz grains (Fig. 3a), suggesting dominant dynamic recrystallization of bulging. In most of the mylonites, subgrain boundaries in quartz grains are commonly observed (Fig. 3b–d), indicating that dynamic recrystallization is mainly driven by subgrain rotation. Moreover, lobate and amoeboid boundaries are also observed in some samples (Fig. 3e),
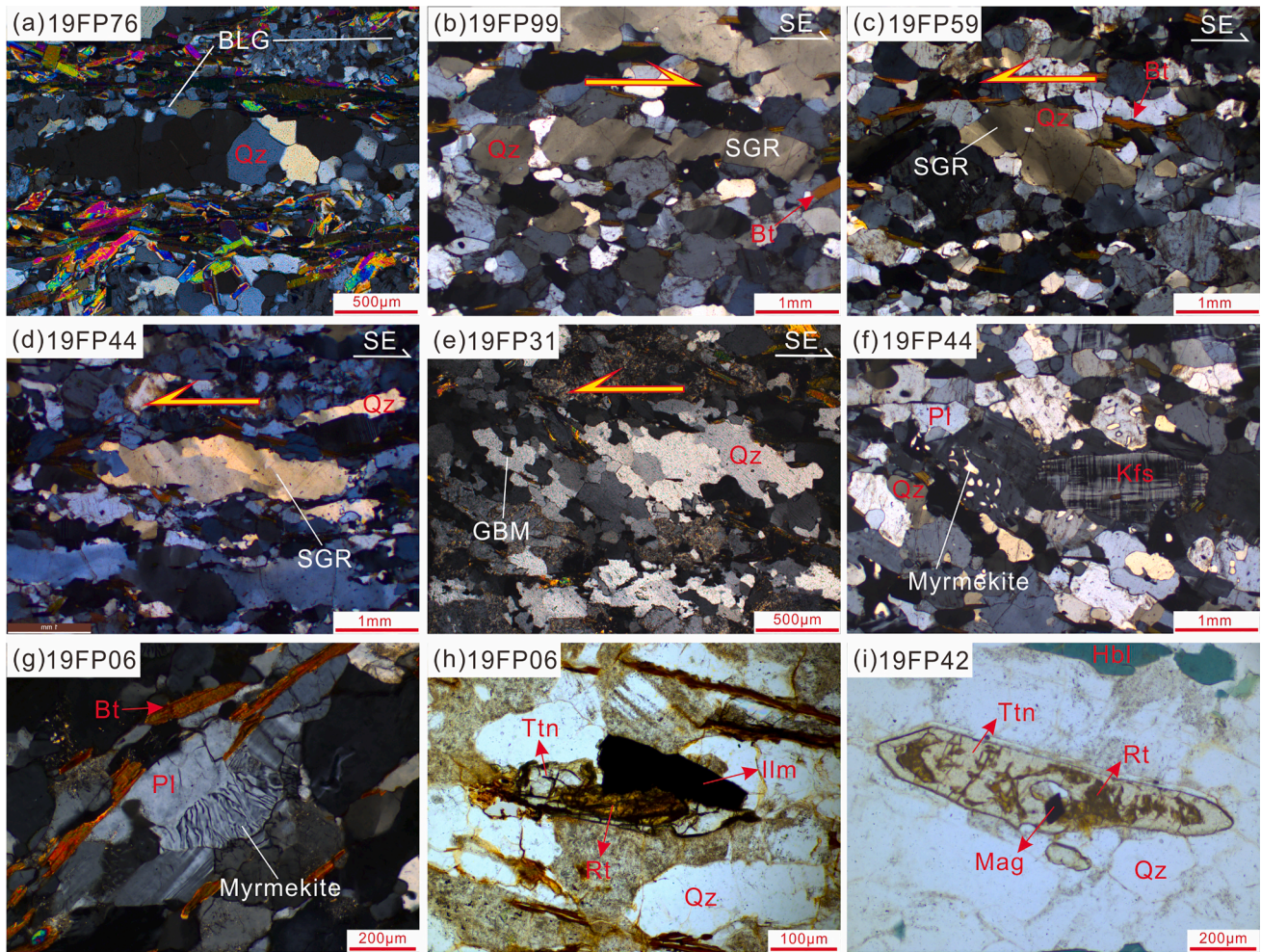
Fig. 3. Microphotographs of the representative mylonite samples from the Longquanguan shear zone. (a) Fine-grained quartz crystals formed rimming the quartz grains, indicating bulging recrystallization. (b–d) Quartz ribbons consist of elongated quartz, and displaying dynamic recrystallization driven by subgrain rotation. The shear sense is dominated by top-to-northwest, with minor of top-to-southeast. (e) Irregular quartz grains display lobate or amoeboid grain boundaries, which is a typical feature of grain boundary migration recrystallization. (f–g) Feldspars are replaced by myrmekites, indicating high-temperature conditions. (h–i) TiO_2-buffering minerals occur in mylonite samples, including rutile, ilmenite, and titanite. Mineral abbreviations are after Whitney and Evans (2010). BLG-bulging recrystallization, SGR-subgrain rotation recrystallization, GBM-grain boundary migration recrystallization.

suggesting dynamic recrystallization activated by grain boundary migration under high temperatures. Quartz oblique foliations (elongation of quartz grains relative to the shear plane) indicate a top-to-northwest sense of shear (Fig. 3c–e), with minor of top-to-southeast (Fig. 3b). In the east of the shear zone, myrmekites are observed developing on the edges of feldspar grains (Fig. 3f–g), indicating a higher thermal condition on dynamic deformation (e.g., Jessell, 1987; Passchier and Trouw, 2005; Stipp et al., 2002; Tullis and Yund, 1987). TiO_2-buffering minerals such as rutile, titanite, and ilmenite appear in most mylonite samples (Fig. 3h–i; Table 1). Quartz ribbons in all 25 mylonite samples were selected for cathodoluminescence (CL) imaging and Ti concentration analyses, among which four samples (LQG03, LQG31, LQG49, and LQG43) were chosen for hornblende and mica $^{40}Ar/^{39}Ar$ dating.

4. Analytical methods

Before measuring Ti concentration, the quartz in the samples was taken cathodoluminescence (CL) images to reveal potential zoning in Ti concentration. CL imaging was conducted on a Tescan Integrated Mineral Analyzer (TIMA) mineralogy system at the Key Laboratory of Orogenic Belts and Crustal Evolution, School of Earth and Space Sciences, Peking University, China. The TIMA measurements were

performed at an accelerating voltage of 20 kV, a spot size of ~ 110 nm, and a working distance of 15 mm.

Analysis of Ti content in quartz was carried out on an Agilent 7900 ICP-MS equipped with a GeoLasPro 193 nm ArF excimer laser at the State Key Laboratory of Ore Deposit Geochemistry, Institute of Geochemistry, Chinese Academy of Science. All mylonite samples for this experiment were prepared as surface-polished sections with a thickness of ~ 100 μm. Laser repetition of 10 Hz, energy density of 10 J/cm^2, and spot size of 44 μm was used. For quantitative calibrations, the external standard of NIST SRM610 was used and analyzed twice every 15 analytical spots. An internal standard-in-dependent calibration strategy, which is based on the normalization of the sum of all metal oxides to 100 wt%, was applied to the calibrations (Liu et al., 2008). Standard glass NIST SRM612 was analyzed to monitor the accuracy of the results, which show that the uncertainties of Ti contents are less than 8%. A natural quartz standard (Audétat et al., 2015) was also analyzed to monitor the accuracy. The detailed analytical procedures are described in Lan et al. (2017, 2018). The Ti content in quartz was summarized in Table 2, and detailed in Table S1.

$^{40}Ar/^{39}Ar$ incremental heating experiment of hornblende and mica was operated on an ARGUS-VI multi-collector mass spectrometer at the Argon Geochronology Laboratory, Oregon State University, USA. Hornblende and mica grains were analyzed in vacuo using a CO_2 laser

Table 2
Summary of Ti contents of quartz in the mylonite and average temperatures determined by different TitaniQ geothermometers.

Profile	Sample	Ti-buffering mineral	Activity	Ti content (ppm)	Average temperatures (°C)		
					Wark and Watson (2006)	Thomas et al. (2010) P = 7kbar	Huang and Audétat (2012) P = 7kbar
Changchengling-Yinchaoshi	LQG19	Rt	1.0	3.37–5.13	474	444	548
	19FP33	Ttn, Ilm	0.8	3.46–4.72	482	451	541
	19FP31	Rt, Ttn	1.0	3.50–5.55	476	445	549
	LQG03	Ttn	0.8	5.01–6.47	505	472	565
	19FP06	Rt, Ttn, Ilm	1.0	3.83–6.52	483	452	558
	19FP01	Rt	1.0	3.77–4.84	471	441	544
Shizui-Muqiao	LQG38	None	0.6	5.24–8.61	539	503	579
	LQG34	None	0.6	5.24–7.00	531	495	570
	LQG31	Ttn	0.8	4.79–6.02	500	467	560
	LQG26	Ttn	0.8	4.79–7.03	516	481	576
Menxianshi-Taohuajie	LQG53	Ttn	0.8	4.49–4.95	492	460	551
	LQG52	Ilm	0.8	4.74–5.96	501	468	561
	LQG49	None	0.6	4.96–5.80	521	486	560
	LQG43	Ttn	0.8	6.23–7.99	519	485	580
Wuqiang-Xiyangdao	19FP47	Ilm	0.8	2.01–2.33	443	415	499
	19FP52	Rt	1.0	1.92–3.10	440	413	510
	19FP53	Rt	1.0	4.05–5.47	478	447	551
	19FP59	None	0.6	4.17–5.21	513	479	552
	19FP42	Rt	1.0	6.55–7.80	507	473	584
	19FP44	Ilm	0.8	9.85–13.35	557	519	621
Mingchawan-Yushuping	19FP76	None	0.6	1.72–2.66	461	432	500
	19FP86	Rt, Ttn, Ilm	1	3.23–5.56	472	442	546
	19FP89	Ttn, Ilm	0.8	5.57–6.85	510	476	571
	19FP99	Ilm	0.8	6.70–8.53	524	489	585
	19FP104	Ilm	0.8	8.31–12.03	553	515	616

Table 3
Summary of ages of hornblende and mica crystals determined by $^{40}Ar/^{39}Ar$ incremental heating experiment.

		Plateau						Total Fusion	Normal Isochron		Inverse Isochron	
Sample	Material	Age ± 2σ (Ma)	^{39}Ar(%)	K/Ca ± 2σ	MSWD	n	N	Age ± 2σ (Ma)	Age ± 2σ (Ma)	MSWD	Age ± 2σ (Ma)	MSWD
LQG03	Hornblende	1802 ± 6	57.69	0.145 ± 0.004	2.09	8	34	1772 ± 6	1815 ± 11	1.29	1812 ± 11	1.28
LQG03	Biotite	1827 ± 4	66.61	2.47 ± 0.77	3.3	13	39	1781 ± 3	1830 ± 8	3.68	1828 ± 8	3.74
LQG31	Hornblende	1850 ± 4	100.00	0.125 ± 0.005	0.7	34	34	1851 ± 7	1857 ± 5	0.67	1850 ± 5	0.76
LQG49	Muscovite	1803 ± 3	91.95	0.2 ± 0.3	1.24	31	37	1805 ± 3	1804 ± 3	0.83	1801 ± 3	0.71
LQG43	Hornblende	1823 ± 5	100.00	0.178 ± 0.006	1.22	34	34	1821 ± 7	1875 ± 18	2.78	1824 ± 5	0.86
LQG43	Biotite	1783 ± 4	50.64	12.0 ± 5.7	7.9	10	54	1763 ± 3	1784 ± 11	9.07	1778 ± 10	8

with an initial low-power preheating step. All displayed age results were normalized to the FCT-NM age of 28.201 ± 0.023 Ma (Kuiper et al., 2008), calculated using the decay constant (5.463 ± 0.107 × 10^{-10} a^{-1}) and Equations of Min et al. (2000). Ages and uncertainties were calculated using the ArArCALC software (Koppers, 2002). The general methods have been detailed in Balbas et al. (2016). A summary of $^{40}Ar/^{39}Ar$ dating is exhibited in Table 3, and the whole data is available in Table S2.

5. Results

5.1. Ti concentration of quartz and TitaniQ geothermometry

Ti concentration of quartz can be reset during dynamic recrystallization (e.g., Cross et al., 2015; Grujic et al., 2011; Nachlas et al., 2014), and the CL imaging of quartz can often reflect its Ti concentration variety (Kohn and Northrup, 2010; Spear and Wark, 2009; Wark and Watson, 2006). In mylonite samples from the Longquanguan shear zone, CL images of quartz ribbons show no clear zonation (Fig. 4), possibly indicating an equilibrium during the dynamic recrystallization. Three to ten spots were analyzed on quartz ribbons in each mylonite sample (Table S1), and temperatures of each of them were calculated using three different versions of TitaniQ geothermometers (Huang and Audétat, 2012; Thomas et al., 2015; Wark and Watson, 2006). In the computation, TiO$_2$ activity (a_{TiO2}) of the rock should be taken carefully.

The a_{TiO2} in the rutile-absent system was expected to range from 0.6 to 1 (e.g., Cross et al., 2015; Ghent and Stout, 1984; Menegon et al., 2011). In this paper, based on the presence of rutile, ilmenite, titanite, and absence of TiO$_2$-buffering minerals, the a_{TiO2} was set to be 1.0, 0.8, 0.8, and 0.6, respectively (e.g., Ghent and Stout, 1984; Peterman and Grove, 2010; Menegon et al., 2011; Spear et al., 2012). It is known that errors of ±0.2 of a_{TiO2} may translate to temperature errors below ±30 °C (e.g., Cross et al., 2015; Kohn and Northrup, 2010; Wark and Watson, 2006). The pressure conditions of ductile deformation were mainly set to be 7 kbar, based on the pressure values calculated by Li and Qian (1991). To investigate the pressure effect on temperature conditions of ductile deformation, other pressure values (e.g., 5 kbar and 10 kbar) were also considered for comparison (Figs. S1 and S2, Table S1).

Along the northern Changchengling-Yinchaoshi profile, Ti content of quartz in different samples is relatively homogeneous (Fig. 5a). From the west to the east, samples LQG19, 19FP33, 19FP31, LQG03, 19FP06, and 19FP01 yield Ti content (ppm) of 3.37–5.13, 3.46–4.72, 3.50–5.55, 5.01–6.47, 3.83–6.52, and 3.77–4.84, respectively (Tables 2, S1). Correspondingly, temperatures calculated by the TitaniQ geothermometry are relatively consistent (Fig. 6a), with average temperatures (°C) of 474, 482, 476, 505, 483, and 471, respectively (Wark and Watson, 2006); or 444, 451, 445, 472, 452, and 441, respectively (Thomas et al., 2010); or 548, 541, 549, 565, 558, and 544, respectively (Huang and Audétat, 2012).

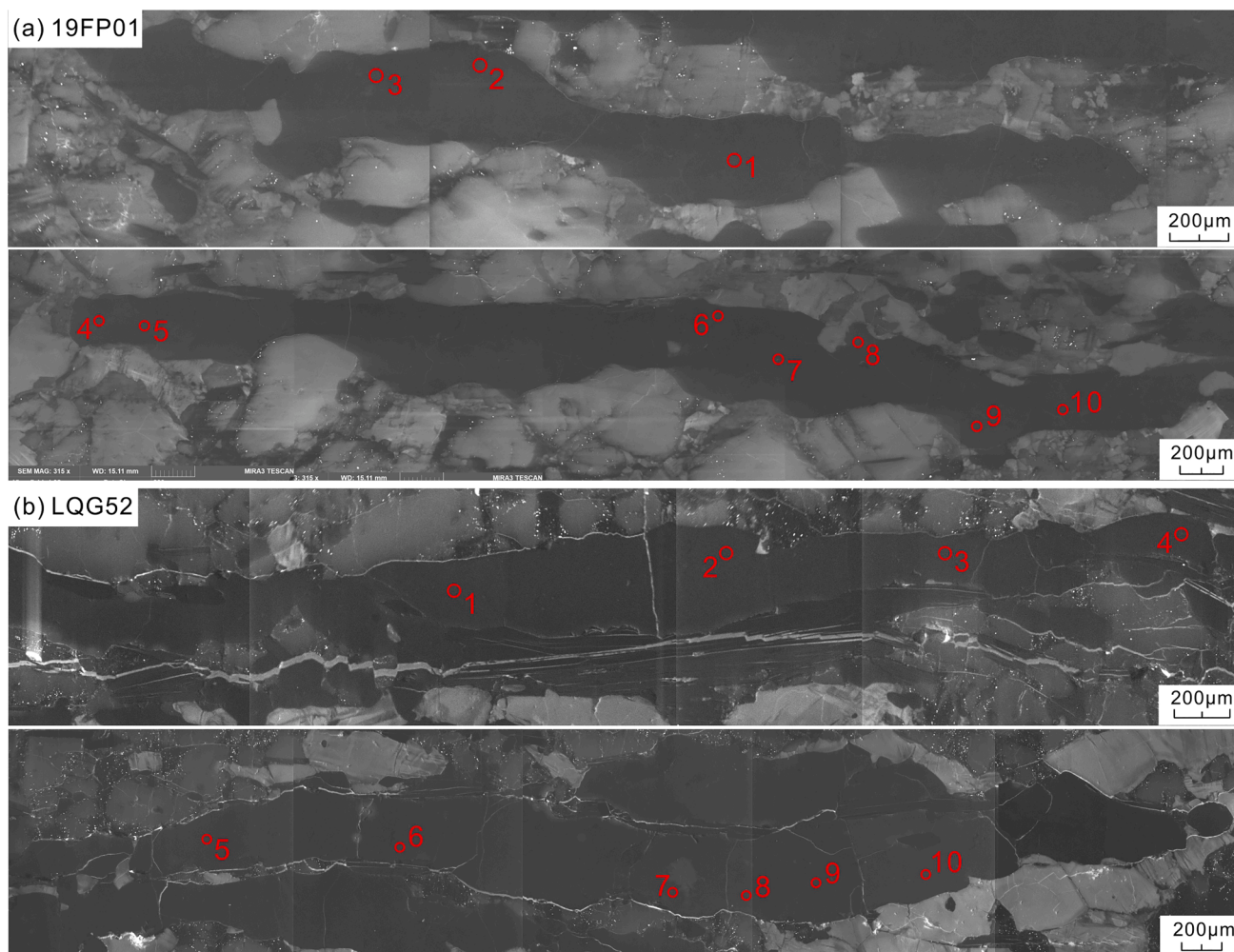In the Shizui-Muqiao profile, Ti content of quartz in different samples

Fig. 4. Representative cathodoluminescence (CL) image of the quartz ribbon. The red circle and red number represent the analytical location and corresponding spot number for Ti content in quartz, respectively.

is relatively homogeneous (Fig. 5b). From the west to the east, samples LQG38, LQG34, LQG31, and LQG26 yield Ti content (ppm) of 5.24–8.61, 5.24–7.00, 4.79–6.02, and 4.79–7.03, respectively (Tables 2, S1). Their temperatures estimated by the TitaniQ geothermometry are also relatively consistent (Fig. 6b), with average temperatures (°C) of 539, 531, 500, and 516, respectively (Wark and Watson, 2006); or 503, 495, 467, and 481, respectively (Thomas et al., 2010); or 579, 570, 560, and 576, respectively (Huang and Audétat, 2012).

In the Menxianshi-Taohuajie profile, Ti element of quartz displays homogeneous concentration in different samples (Fig. 5c). From the west to the east, samples LQG53, LQG52, LQG49, and LQG43 display Ti content (ppm) of 4.49–4.95, 4.74–5.96, 4.96–5.80, and 6.23–7.99, respectively (Tables 2, S1). The calculated temperatures are statistically indistinguishable (Fig. 6c), with average temperatures (°C) of 492, 501, 521, and 519, respectively (Wark and Watson, 2006); or 460, 468, 486, and 485, respectively (Thomas et al., 2010); or 551, 561, 560, and 580, respectively (Huang and Audétat, 2012).

In the profile Wuqiang-Xiyangdao, Ti content of quartz varies from sample to sample (Fig. 5d). From the west to the east, samples 19FP47, 19FP52, 19FP53, 19FP59, 19FP42, and 19FP44 yield increasing Ti content (ppm) of 2.01–2.33, 1.92–3.10, 4.05–5.47, 4.17–5.21, 6.55–7.80, 9.85–13.35, respectively, from the west to the east (Tables 2, S1). Their corresponding temperatures computed by the TitaniQ geothermometry display a similar increasing trend (Fig. 6d), with average temperatures (°C) of 443, 440, 478, 513, 507, and 557, respectively (Wark and Watson, 2006); or 415, 413, 447, 479, 473, and 519,

respectively (Thomas et al., 2010); or 499, 510, 551, 552, 584, and 621, respectively (Huang and Audétat, 2012).

A similar trend is found in the southern Mingchawan-Yushuping profile (Fig. 5e). From the west to the east, samples 19FP76, 19FP86, 19FP89, 19FP99, and 19FP104 show an increase in Ti concentration (ppm) in quartz of 1.72–2.66, 3.23–5.56, 5.57–6.85, 6.70–8.53, 8.31–12.03, respectively (Tables 2, S1). Temperatures estimated by TitaniQ geothermometry also show an increasing trend from the west to the east (Fig. 6e), with average temperatures (°C) of 461, 472, 510, 524, and 553, respectively (Wark and Watson, 2006); or 432, 442, 476, 489, and 515, respectively (Thomas et al., 2010); or 500, 546, 571, 585, and 616, respectively (Huang and Audétat, 2012).

5.2. $^{40}Ar/^{39}Ar$ geochronology

Results of $^{40}Ar/^{39}Ar$ geochronological data are summarized in Table 3, while the full data set is listed in Table S2. The age spectra are shown in Fig. 7, and plateaus typically include released $^{39}Ar_K$ between 50.64% and 100%.

In sample LQG03 (with the deformational temperature of 505 °C; Wark and Watson, 2006), the hornblende exhibits a plateau age of 1802 ± 6 Ma (MSWD = 2.09) with 57.69% ^{39}Ar released (Fig. 7a), which is consistent with the normal isochron age of 1815 ± 11 Ma (MSWD = 1.29) and the inverse isochron age of 1812 ± 11 Ma (MSWD = 1.28). The biotite displays a plateau age of 1827 ± 4 Ma (MSWD = 3.3) with 66.61% ^{39}Ar released (Fig. 7b), which is accordant with the normal
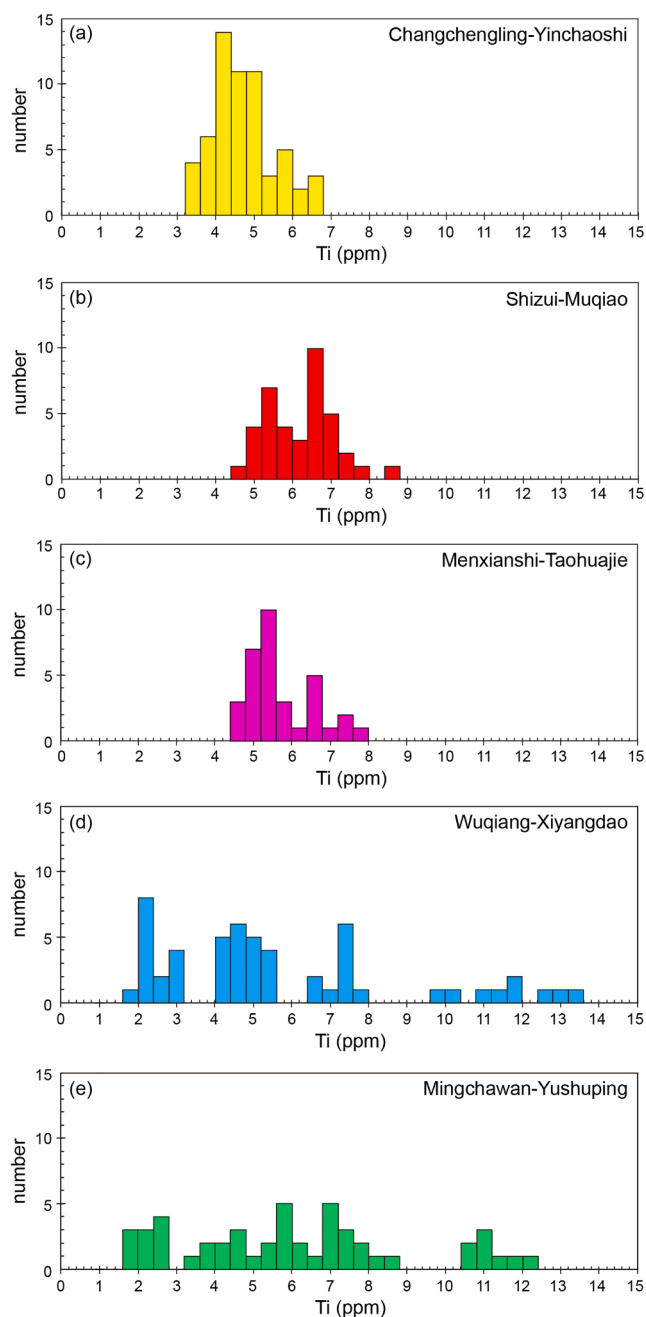
Fig. 5. Histograms of Ti content (in ppm) of quartz ribbons in the mylonite of the five profiles, Longquanguan shear zone.

isochron age of 1830 ± 8 Ma (MSWD = 3.68) and inverse isochron age of 1828 ± 8 Ma (MSWD = 3.74).

In sample LQG31 (with the deformational temperature of 500 °C; Wark and Watson, 2006), the hornblende yields a plateau age of 1850 ± 4 Ma (MSWD = 0.7), comprising 100% of the ^{39}Ar released (Fig. 7c). The normal isochron age and inverse isochron age are 1857 ± 5 Ma (MSWD = 0.67), and 1850 ± 5 Ma (MSWD = 0.76), respectively, which are almost identical to the plateau age.

In sample LQG49 (with the deformational temperature of 520 °C; Wark and Watson, 2006), the muscovite gives a plateau age of 1803 ± 3 Ma (MSWD = 1.24), consisting 91.95% of the ^{39}Ar released (Fig. 7d). The normal isochron age and inverse isochron age are 1804 ± 3 Ma (MSWD = 0.83) and 1801 ± 3 Ma (MSWD = 0.71), respectively, which are almost identical to the plateau age.

In sample LQG43 (with the deformational temperature of 520 °C;

Wark and Watson, 2006), the hornblende shows a plateau age of 1823 ± 5 Ma (MSWD = 1.22), comprising 100% of the ^{39}Ar released (Fig. 7e). The normal isochron age and inverse isochron age are 1875 ± 18 Ma (MSWD = 2.78) and 1824 ± 5 Ma (MSWD = 0.86), respectively. The inverse isochron age is consistent with the plateau age. The biotite displays a plateau age of 1783 ± 4 Ma (MSWD = 7.9), with 50.64% ^{39}Ar released (Fig. 7f). The normal isochron age and inverse isochron age are 1784 ± 11 Ma (MSWD = 9.07) and 1778 ± 10 Ma (MSWD = 8), respectively, which are almost identical to the plateau age.

6. Discussion

6.1. Temperature conditions of ductile deformation

Temperature is one of the critical factors that affect the rheology of the ductile deformation, and thus the formation of microfabrics. In this work, three versions of TitaniQ geothermometers were applied to assess the temperature conditions. The important procedure is to set the a_{TiO2} as aforementioned in using this thermometer. Wark and Watson (2006) calibrated the TitaniQ geothermometer in the presence of rutile (a_{TiO2} = 1), and pointed out that the thermometer can also be applied to rutile-absent systems if a_{TiO2} is well constrained. In rutile-absent rocks, a_{TiO2} is speculated to range from 0.6 to 1.0, and a_{TiO2} is always higher than 0.8 for felsic amphibolite-facies rocks (Ghent and Stout, 1984). In many granites, a_{TiO2} is above 0.6 (Wark et al., 2007; Wark and Watson, 2006). Therefore, we set the a_{TiO2} to be 1, 0.8, 0.8, and 0.6, respectively, based on the presence of rutile, ilmenite, titanite, and absence of Ti-buffering minerals, which are in accordance with a_{TiO2} estimates in other similar rocks (e.g., Ghent and Stout, 1984; Peterman and Grove, 2010; Menegon et al., 2011; Spear et al., 2012). For errors of ±0.2 of a_{TiO2}, temperature errors are, at most, ±30 °C (e.g., Cross et al., 2015; Kohn and Northrup, 2010; Wark and Watson, 2006). Additionally, setting the value of pressure is also quite important, and ±1 kbar difference will generate variations of ~±20 °C in temperature computation (Thomas et al., 2010). In this work, we take the pressure conditions to be 7 kbar based on the pressure conditions estimated by Li and Qian (1991). Furthermore, considering that the ductile shear zones usually develop at the depths of ~12–35 km (e.g., Fossen and Cavalcante, 2017), and the average pressure gradient is ~0.30 kbar/km (Spear, 1993), 5 kbar and 10 kbar were used as alternatives to derive temperature conditions for comparison (Figs. S1 and S2). In general, calculated temperature profiles with pressure input of 5 kbar, 7 kbar, and 10 kbar exhibit the same trend (Figs. 6, S1, S2).

The temperature profiles computed by the three different TitaniQ thermometers are fairly similar (Fig. 6). However, temperatures estimated by the thermometer of Huang and Audétat (2012) are 50–100 °C higher than those by Wark and Watson (2006) and Thomas et al. (2010). Such temperature differences are not uncommon in deformation temperature studies (e.g., Cavalcante et al., 2014; 2018;; Cross et al., 2015; Nachlas et al., 2014). Huang and Audétat (2012) concluded that this discrepancy between their calibration and that of Thomas et al. (2010) possibly resulted from different growth rates of quartz grains. Given the growth rate of quartz was 10–50 times faster in the work of Thomas et al. (2010) than that of Huang and Audétat (2012), Huang and Audétat (2012) speculated that a higher growth rate artificially accelerates the incorporation of titanium in quartz, which would make the calibration tend to yield lower temperatures. On the contrary, Thomas et al. (2015) attributed the temperature differences to out-of-equilibrium in the experimental runs of Huang and Audétat (2012). Therefore, we conservatively applied the middle temperature values obtained from the Wark and Watson (2006) geothermometer.

The geothermometric results show that the three northern profiles (Changchengling-Yinchaoshi, Shizui-Muqiao, and Menxianshi-Taohuajie) all yielded similar values of ~500 °C (Fig. 6a–c). Nevertheless, the two southern profiles (Wuqiang-Xiyangdao and Mingchawan-Yushuping) show eastward increasing temperatures from ~450 °C to
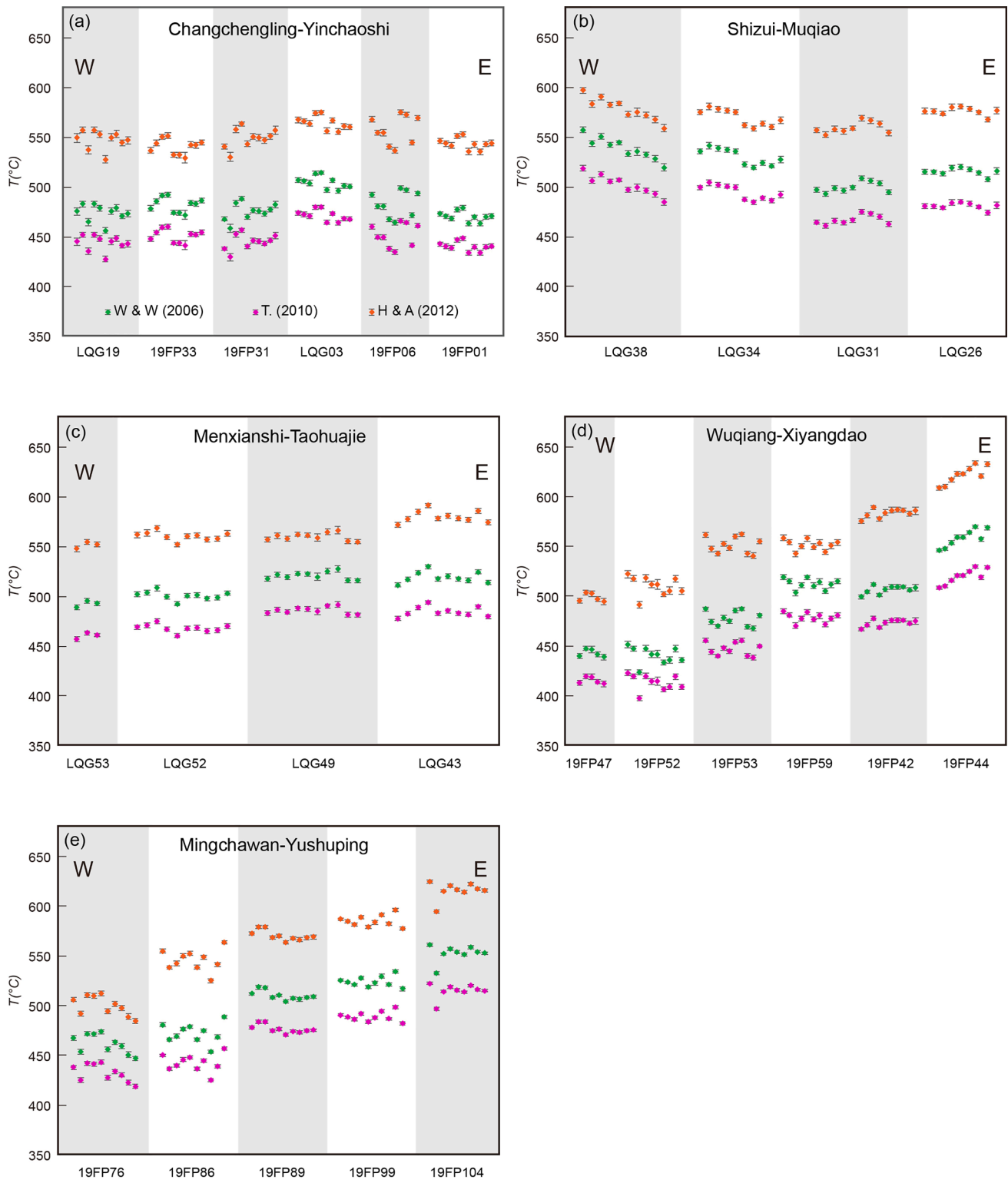
Fig. 6. Distribution of estimated temperatures of the mylonites in the five profiles, Longquanguan shear zone, determined by TitaniQ geothermometers of Wark and Watson (2006), Thomas et al. (2010) and Huang and Audétat (2012), respectively. The pressure was set to be 7 kbar, and the error bars were estimated by the analytical uncertainty.

~550 °C (Fig. 6d–e, 8), which is first reported in the Longquanguan shear zone. Such an eastward temperature increase is evidenced by the spatial occurrence of distinctive microstructures and their associated mechanisms of dynamic recrystallization: the core-mantle structure (bulging, Fig. 3a) is mostly observed along the western side of the zone; quartz subgrains (subgrain rotation, Fig. 3b–d) are ubiquitously

discovered in the main body of the zone; and the lobate and serrated grain boundaries of quartz (Fig. 3e) that may relate to grain boundary migration as well as the development of myrmekites around feldspar edges (Fig. 3f–g) along the eastern front of the zone, these demonstrate that there is a temperature gradient increasing eastward from ~400 °C to >550 °C (e.g., Jessell, 1987; Passchier and Trouw, 2005; Stipp et al.,
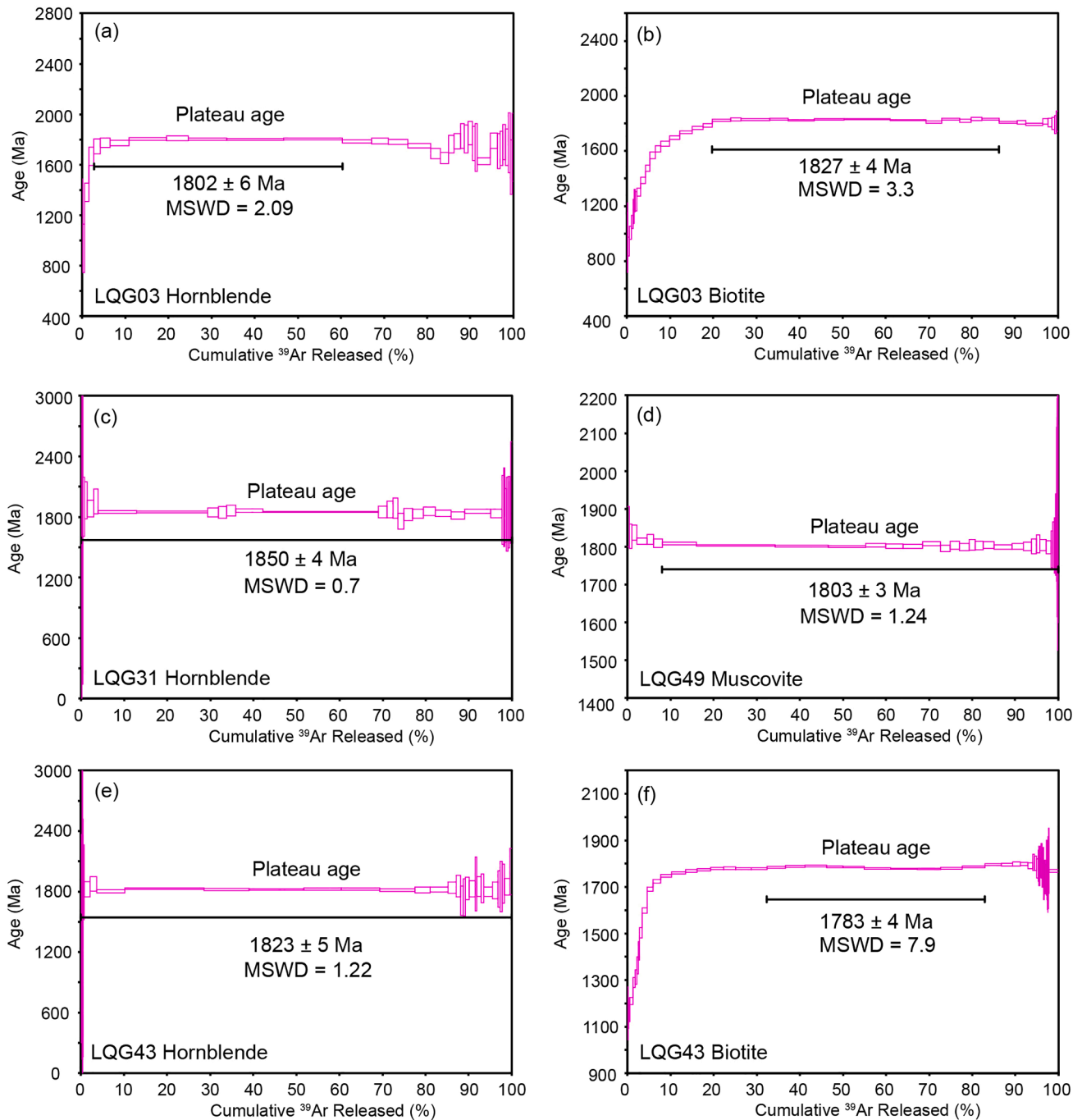
Fig. 7. $^{40}Ar/^{39}Ar$ age spectra of hornblende and mica from the mylonite in the Longquanguan shear zone.

2002; Tullis and Yund, 1987).

Accordingly, we argue that this temperature gradient indeed exists rather than introduced errors via setting a_{TiO2} and pressure values, based on integrated temperature data and observed microstructures. In fact, similar temperature trend has been discovered in many shear zones (e. g., Stipp et al., 2002; Zhang et al., 2018), which was commonly attributed to a heat source of intrusions. However, since no synchronous intrusions were found near/within the Longquanguan shear zone, such a temperature gradient is possibly related to the geothermal gradient between the hanging wall (the Wutai Complex) and the footwall (the Fuping Complex) of the shear zone. The shear zone narrows out to the north, and the temperature gradient smears out northward (Fig. 8), which is likely caused by differential erosion/denudation of this shear zone, that thus more and rather complete litho-structural units are

exposed in the southern section. Combined with the sampling length of the two southern sections of ~11 km, an average value of dipping angle of ~25°, and temperature differences of 114 and 92 °C, a temperature gradient of ductile deformation was calculated to be approximately 20–25 °C/km.

6.2. Timing of ductile deformation and tectonic significance

The closure temperature is critical to understand thermochronological data (Dodson, 1973). Based on the calculated or measured values for $^{40}Ar/^{39}Ar$ system, closure temperature of 490–570 °C for hornblende (Harrison, 1982), 405–425 °C for muscovite (Harrison et al., 2009), and 345–280 °C for biotite (Grove and Harrison, 1996; Harrison et al., 1985) were adopted in this work. The analyzed mylonite samples yielded
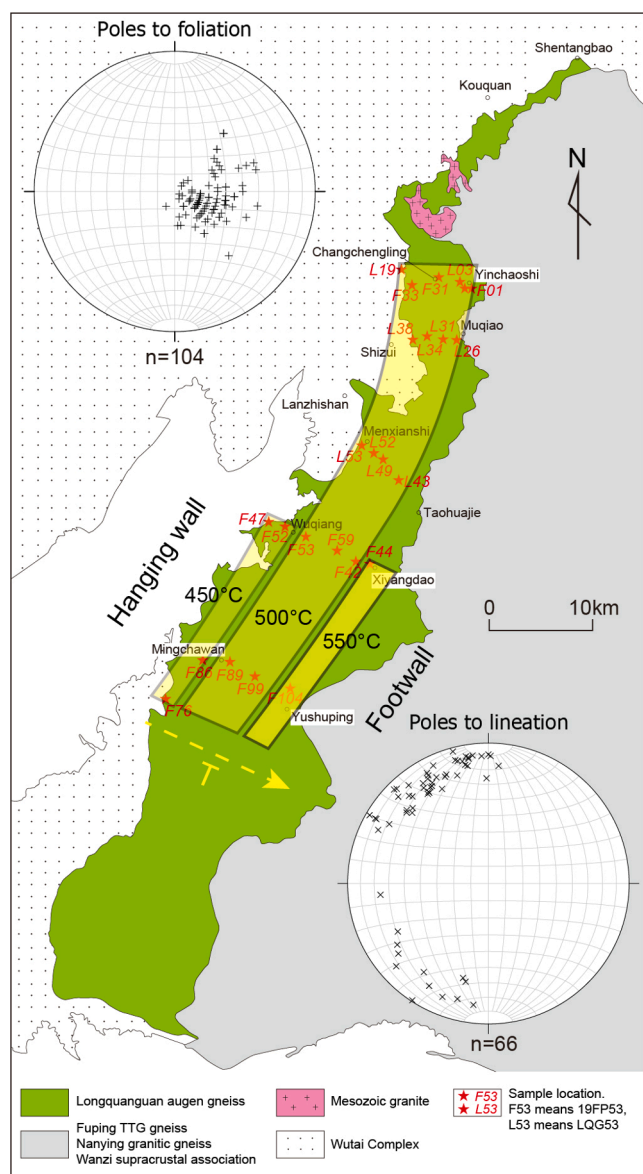
Fig. 8. Temperature gradient of the Longquanguan shear zone, determined by the TitaniQ geothermometer of Wark and Watson (2006).

^{40}Ar/^{39}Ar age of hornblende of 1850–1802 Ma (LQG03, LQG31, and LQG43), ^{40}Ar/^{39}Ar age of muscovite of 1803 Ma (LQG49), and ^{40}Ar/^{39}Ar age of biotite of 1827–1783 Ma (LQG03 and LQG43), respectively. It is noted that the deformational temperature conditions (500–521 °C) determined by the Wark and Watson (2006) geothermometer of the dating mylonite samples (LQG03, LQG31, LQG43, LQG49) are similar to the closure temperature of the ^{40}Ar/^{39}Ar system of hornblende, but higher than the closure temperature of ^{40}Ar/^{39}Ar system of muscovite and biotite. Therefore, the hornblende ^{40}Ar/^{39}Ar ages of 1850–1802 Ma possibly represent the age of ductile deformation, whereas the ^{40}Ar/^{39}Ar ages of muscovite and biotite of 1827–1783 Ma are considered as cooling ages. The hornblende ^{40}Ar/^{39}Ar age ranges almost 50 Ma, possibly indicating complex or heterogeneous deformation timing along and across the regional-scale shear zone. These two groups of ages are similar and partially overlapped, possibly indicating a rapid cooling history, which is consistent with the relatively rapid cooling/exhumation of the TNCO (e.g., Liu et al., 2021a). The unusual hornblende ^{40}Ar/^{39}Ar age of sample LQG03 is about ~25 Ma younger than its biotite ^{40}Ar/^{39}Ar age, which could be caused by analytical errors or possible rapid cooling.

Again, ^{40}Ar/^{39}Ar ages of biotite and muscovite are essentially cooling ages. However, we may argue that these ages record a short-span, rapid cooling process of the mid-lower crust during progressive deformation over the temperature range of ~300–430 °C. Given the fact that all the minerals used for age dating are fabric-forming minerals: observed hornblende and micas participated in the formation of foliation and lineation (Figs. 2 and 3), and considering the similarity of these ages, it is very likely that we are looking at a scenario that the ductile fabrics frozen in along with their temporal signatures during the fast exhumation of the Trans-North China Orogen over the low-*T* range. Therefore, ^{40}Ar/^{39}Ar ages of biotite and muscovite of 1823–1785 Ma record the late-phase progressive deformation during the aggregation of the Eastern and Western Blocks.

In fact, similar ages of deformation were reported in the Longquanguan shear zone. Zhao et al. (2006) obtained three age peaks (1877–1846 Ma, 1812–1782 Ma, and 1725 Ma) by EPMA U-Th-Pb dating of monazite from *syn*-deformational granite, which were interpreted as the ages of deformation, uplift, and the late fluid activity, respectively. Furthermore, the ductile deformation age (1850–1802 Ma) in this contribution is also in accordance with other metamorphic ages (1.89–1.80 Ga) in the Fuping Complex (e.g., Guan et al., 2002; Liu et al., 2002, 2019; Zhao et al., 2002a; 2002b;; Xia et al., 2006; Meng et al., 2017; Qian et al., 2018). Similar metamorphic/deformational age possibly indicates that the Longquanguan shear zone suffered ductile deformation synchronously with the metamorphism of the Fuping Complex, both of which occurred during the collision event between the Western and Eastern Blocks. In this event, the Longquanguan shear zone experienced a heterogeneous deformation that occurred at different depths between the hanging wall and footwall, then followed by a quick exhumation.

7. Conclusion

(1) The Longquanguan shear zone experienced heterogeneous dynamic recrystallization, dominated by subgrain rotation recrystallization. The S-C fabrics suggest a dominant shear sense of top-to-NW.

(2) Ti contents in quartz are homogeneous in the three northern profiles (3.37–6.52 ppm, Changchengling-Yinchaoshi; 4.79–8.61 ppm, Shizui-Muqiao; and 4.49–7.99 ppm, Menxianshi-Taohuajie). But in the two southern sections, the Ti content increases eastward (1.92–13.35 ppm, Wuqiang-Xiyangdao; and 1.72–12.03 ppm, Mingchawan-Yushuping).

(3) Application of the TitaniQ geothermometer indicates that the temperature conditions of ductile deformation are homogeneous in the three northern profiles (474–505 °C, Changchengling-Yinchaoshi; 500–539 °C, Shizui-Muqiao; and 492–521 °C, Menxianshi-Taohuajie), whereas the temperature conditions in the two southern sections show eastward increasing trend (440–557 °C, Wuqiang-Xiyangdao; and 461–553 °C, Mingchawan-Yushuping). A temperature gradient is estimated to be 20–25 °C/km, which possibly relates to the geothermal gradient between the hanging wall (the Wutai Complex) and the footwall (the Fuping Complex).

(4) ^{40}Ar/^{39}Ar dating of hornblende and mica constrain the ductile deformation to be from 1850 to 1802 Ma, and followed diachronously by a rapid cooling between 1827 and 1783 Ma.

(5) The Longquanguan shear zone records ductile deformation between the Fuping and Wutai Complexes, and followed by a quick exhumation, which occurred during the collision event between the Eastern and Western Blocks in the Late Paleoproterozoic.

Declaration of Competing Interest

The authors declare that they have no known competing financial interests or personal relationships that could have appeared to influence

the work reported in this paper.

Acknowledgments

Appendix A. Supplementary data

Supplementary data to this article can be found online at https://doi.org/10.1016/j.precamres.2021.106217.

References

Ashley, K.T., Webb, L.E., Spear, F.S., Thomas, J.B., 2013. P-T-D histories from quartz: a case study of the application of the TitaniQ thermobarometer to progressive fabric development in metapelites. Geochem. Geophys. Geosyst. 14, 3821–3843.

Audétat, A., Garbe-Schoenberg, D., Kronz, A., Pettke, T., Rusk, B., Donovan, J.J., Lowers, H.A., 2015. Characterisation of a natural quartz crystal as a reference material for microanalytical determination of Ti, Al, Li, Fe, Mn, Ga and Ge. Geostand. Geoanal. Res. 39, 171–184.

BALBAS, A., KOPPERS, A.A., KENT, D.V., KONRAD, K., CLARK, P.U., 2016. IDENTIFICATION OF THE SHORT-LIVED SANTA ROSA GEOMAGNETIC EXCURSION IN LAVAS ON FLOREANA ISLAND (GALAPAGOS) BY ⁴⁰AR/³⁹AR GEOCHRONOLOGY. GEOLOGY 44, 359–362.

Bestmann, M., Pennacchioni, G., 2015. Ti distribution in quartz across a heterogeneous shear zone within a granodiorite: the effect of deformation mechanism and strain on Ti resetting. Lithos 227, 37–56.

Cao, S.Y., Liu, J.L., Hu, L., 2007. Micro- and submicrostructural evidence for high-temperature brittle-ductile transition deformation of hornblende: case study of high-grade mylonites from Diancangshan, western Yunnan. Sci. China Series D-Earth Sci. 50, 1459–1470.

Cavalcante, C., Lagoeiro, L., Fossen, H., Egydio-Silva, M., Morales, L.F.G., Ferreira, F., Conte, T., 2018. Temperature constraints on microfabric patterns in quartzofeldsphatic mylonites, Ribeira belt (SE Brazil). J. Struct. Geol. 115, 243–262.

Cavalcante, G.C.G., Vauchez, A., Merlet, C., Egydio-Silva, M., Bezerra de Holanda, M.H., Boyer, B., 2014. Thermal conditions during deformation of partially molten crust from TitaniQ geothermometry: rheological implications for the anatectic domain of the Aracuaui belt, eastern Brazil. Solid Earth 5, 1223–1242.

Cottle, J.M., Larson, K.P., Kellett, D.A., 2015. How does the mid-crust accommodate deformation in large, hot collisional orogens? A review of recent research in the Himalayan orogen. J. Struct. Geol. 78, 119–133.

Cross, A.J., Kidder, S., Prior, D.J., 2015. Using microstructures and TitaniQ thermobarometry of quartz sheared around garnet porphyroclasts to evaluate microstructural evolution and constrain an Alpine Fault Zone geotherm. J. Struct. Geol. 75, 17–31.

Dodson, M.H., 1973. Closure temperature in cooling geochronological and petrological systems. Contrib. Miner. Petrol. 40, 259–274.

Fossen, H., 2010. Extensional tectonics in the North Atlantic Caledonides: a regional view. Geological Society, London, Special Publications, 767–793.

Fossen, H., Cavalcante, G.C.G., 2017. Shear zones – a review. Earth Sci. Rev. 171, 434–455.

Ghent, E.D., Stout, M.Z., 1984. TiO₂ activity in metamorphosed pelitic and basic rocks-principles and applications to metamorphism in southeastern Canadian Cordillera. Contrib. Miner. Petrol. 86, 248–255.

Godin, L., Grujic, D., Law, R.D., Searle, M.P., 2006. Channel flow, ductile extrusion and exhumation in continental collision zones: an introduction. Geological Society, London, Special Publications, 1–23.

Grove, M., Harrison, T.M., 1996. ⁴⁰Ar* diffusion in Fe-rich biotite. Am. Mineral. 81, 940–951.

Grujic, D., Stipp, M., Wooden, J.L., 2009. Thermometry of quartz mylonites. Geochim. Cosmochim. Acta 73, A472–472.

Grujic, D., Stipp, M., Wooden, J.L., 2011. Thermometry of quartz mylonites: Importance of dynamic recrystallization on Ti-in-quartz reequilibration. Geochem. Geophys. Geosyst. 12, 6.

Guan, H., Sun, M., Wilde, S.A., Zhou, X.H., Zhai, M.G., 2002. SHRIMP U-Pb zircon geochronology of the Fuping Complex: implications for formation and assembly of the North China Craton. Precambr. Res. 113, 1–18.

Haertel, M., Herwegh, M., Pettke, T., 2013. Titanium-in-quartz thermometry on synkinematic quartz veins in a retrograde crustal-scale normal fault zone. Tectonophysics 608, 468–481.

Han, B.F., Xu, Z., Ren, R., Li, L.L., Yang, J.H., Yang, Y.H., 2012. Crustal growth and intracrustal recycling in the middle segment of the Trans-North China Orogen, North China Craton: a case study of the Fuping Complex. Geol. Mag. 149, 729–742.

Harrison, T.M., 1982. Diffusion of ⁴⁰Ar in hornblende. Contrib. Miner. Petrol. 78, 324–331.

Harrison, T.M., Célérier, J., Aikman, A.B., Hermann, J., Heizler, M.T., 2009. Diffusion of ⁴⁰Ar in muscovite. Geochim. Cosmochim. Acta 73, 1039–1051.

Harrison, T.M., Duncan, I., McDougall, I., 1985. Diffusion of ⁴⁰Ar in biotite: Temperature, pressure and compositional effects. Geochim. Cosmochim. Acta 49, 2461–2468.

He, L.C., Zhang, J., Zhao, G.C., Yin, C.Q., Qian, J.H., Liu, J., Xia, X.G., Zhao, C., 2020. Macro- and microstructural analysis of the Zhujiafang ductile shear zone, Hengshan Complex: Tectonic nature and geodynamic implications of the evolution of Trans–North China orogen. Gological Society of America (in press) doi: 10.1130/B35672.1.

Hirth, G., Tullis, J., 1992. Dislocationcreep regimes in quartz aggregates. J. Struct. Geol. 14, 145–159.

Huang, R.F., Audétat, A., 2012. The titanium-in-quartz (TitaniQ) thermobarometer: A critical examination and re-calibration. Geochim. Cosmochim. Acta 84, 75–89.

Hughes, C.A., Jessup, M.J., Shaw, C.A., Newell, D.L., 2019. Deformation conditions during syn-convergent extension along the Cordillera Blanca shear zone, Peru. Geosphere 15, 1342–1367.

Jessell, M.W., 1987. Grain-boundary migration microstructures in a naturally deformed quartzite. J. Struct. Geol. 9, 1007–1014.

Kohn, M.J., Northrup, C.J., 2010. Taking mylonites' temperatures. Geology 37, 47–50.

Koppers, A.A.P., 2002. ArArCALC-software for ⁴⁰Ar/³⁹Ar age calculations. Computers and Geosciences (UK) 28, 605–619.

Kruhl, J.H., 1998. Prism- and basal-plane parallel subgrain boundaries in quartz: a microstructural geothermobarometer – reply. J. Metamorph. Geol. 16, 142–146.

Kuiper, K.F., Deino, A., Hilgen, F.J., Krijgsman, W., Renne, P.R., Wijbrans, J.R., 2008. Synchronizing rock clocks of Earth history. Science 320, 500–504.

Kusky, T.M., Li, J., 2003. Paleoproterozoic tectonic evolution of the North China Craton. J. Asian Earth Sci. 22, 383–397.

Kusky, T.M., Polat, A., Windley, B.F., Burke, K.C., Dewey, J.F., Kidd, W.S.F., Maruyama, S., Wang, J.P., Deng, H., Wang, Z.S., Wang, C., Fu, D., Li, X.W., Peng, H. T., 2016. Insights into the tectonic evolution of the North China Craton through comparative tectonic analysis: A record of outward growth of Precambrian continents. Earth Sci. Rev. 162, 387–432.

Lan, T.G., Hu, R.Z., Bi, X.W., Mao, G.J., Wen, B.J., Liu, L., Chen, Y.H., 2018. Metasomatized asthenospheric mantle contributing to the generation of Cu-Mo deposits within an intracontinental setting: A case study of the similar to 128 Ma Wangjiazhuang Cu-Mo deposit, eastern North China Craton. J. Asian Earth Sci. 160, 460–489.

Lan, T.G., Hu, R.Z., Fan, H.R., Bi, X.W., Tang, Y.W., Zhou, L., Mao, W., Chen, Y.H., 2017. In-situ analysis of major and trace elements in fluid inclusion and quartz: LA-ICP-MS method and applications to ore deposits. Acta Petrology Sinica 33, 3239–3262 (in Chinese with English abstract).

Law, R.D., 2014. Deformation thermometry based on quartz c-axis fabrics and recrystallization microstructures: a review. J. Struct. Geol. 66, 129–161.

Leloup, P.H., Kienast, J.R., 1993. High-temperature metamorphism in a major strike-slip shear zone: the Ailao Shan—Red River, People's Republic of China. Earth Planet. Sci. Lett. 118, 213–234.

Li, J.H., Qian, X.L., 1991. Study on the Longquanguan shear zone in the northern Taihang mountain. Shanxi Geol. 6, 17–26.

Li, S.Z., Zhao, G.C., Wilde, S.A., Zhang, J., Sun, M., Zhang, G.W., Dai, L.M., 2010. Deformation history of the Hengshan-Wutai-Fuping Complexes: Implications for the evolution of the Trans-North China Orogen. Gondwana Res. 18, 611–631.

Liang, C.Y., Liu, Y.J., Neubauer, F., Bernroider, M., Jin, W., Li, W.M., Zeng, Z.X., Wen, Q. B., Zhao, Y.L., 2015. Structures, kinematic analysis, rheological parameters and temperature-pressure estimate of the Mesozoic Xingcheng-Taili ductile shear zone in the North China Craton. J. Struct. Geol. 78, 27–51.

Liu, J.H., Li, Z.M.G., Zhang, Q.W.L., Zhang, H.C.G., Chen, Y.C., Wu, C.M., 2021a. New ⁴⁰Ar/³⁹Ar geochronology data of the Fuping and Wutai Complexes: further constraints on the thermal evolution of the Trans-North China Orogen. Precambr. Res. 354, 106046.

Liu, J.H., Zhang, Q.W.L., Wang, J., Zhang, H.C.G., Wu, C.M., 2021b. Metamorphic evolution and SIMS U-Pb geochronology of orthopyroxene-bearing high-pressure semipelitic granulite in the Fuping area, middle Trans-North China Orogen. J. Metamorphic Geol. https://doi.org/10.1111/jmg.12580.

Liu, J.H., Zhang, Q.W.L., Zhang, H.C.G., Wang, H.Y.C., Chen, H.X., Pham, V.T., Peng, T., Wu, C.M., 2019. Metamorphic evolution and SHRIMP U-Pb geochronology of mafic granulites with double symplectites in the Fuping metamorphic complex, middle Palaeoproterozoic Trans-North China Orogen. Precambr. Res. 326, 142–154.

Liu, S.W., Pan, Y.M., Li, J.H., Li, Q.G., Zhang, J., 2002. Geological and isotopic geochemical constraints on the evolution of the Fuping Complex, North China Craton. Precambr. Res. 117, 41–56.

Liu, Y.S., Hu, Z.C., Gao, S., Günther, D., Xu, J., Gao, C.G., Chen, H.H., 2008. In situ analysis of major and trace elements of anhydrous minerals by LA-ICP-MS without applying an internal standard. Chem. Geol. 257, 34–43.

Menegon, L., Nasipuri, P., Stünitz, H., Behrens, H., Ravna, E., 2011. Dry and strong quartz during deformation of the lower crust in the presence of melt. Journal of Geophysical Research-Solid Earth (1978–2012) 116 (B10).

Meng, J., Peng, T., Liu, J.H., Zhang, H.C.G., Wang, G.D., Lu, J.S., Chen, H.X., Wang, H.Y. C., Zhang, Q.W.L., Wu, C.M., 2017. Metamorphic evolution and SIMS zircon U-Pb geochronology of mafic granulite and amphibolite enclaves of the Pingyang trondhjemitic pluton, Fuping terrane, North China. Precambr. Res. 303, 75–90.

Min, K., Mundil, R., Renne, P.R., Ludwig, K.R., 2000. A test for systematic errors in $^{40}Ar/^{39}Ar$ geochronology through comparison with U/Pb analysis of a 1.1-Ga rhyolite. Geochim. Cosmochim. Acta 64, 73–98.

Nachlas, W.O., Whitney, D.L., Teyssier, C., Bagley, B., Mulch, A., 2014. Titanium concentration in quartz as a record of multiple deformation mechanisms in an extensional shear zone. Geochem. Geophys. Geosyst. 1374–1397.

Passchier, C.W., Trouw, R.A.J., 2005. Microtectonics, second ed. Springer, Berlin, p. 57.

Pei, L.T., Yang, M., Ma, G.X., Hao, T.P., Bin, J.L., Han, Z.H., 2001. The geological character of the Longquanguan ductile shear zone. Beijing Geology 1–11 (in Chinese with English abstract).

Peng, P., Zhai, M.G., Zhang, H.F., Guo, J.H., 2005. Geochronological constraints on the Paleoproterozoic evolution of the North China craton: SHRIMP zircon ages of different types of Mafic dikes. Int. Geol. Rev. 47, 492–508.

Pennacchioni, G., Menegon, L., Leiss, B., Nestola, F., Bromiley, G., 2010. Development of crystallographic preferred orientation and microstructure during plastic deformation of natural coarse-grained quartz veins. J. Geophys. Res.-Solid Earth 115, B12405.

Peterman, E.M., Grove, M., 2010. Growth conditions of symplectic muscovite + quartz: implications for quantifying retrograde metamorphism in exhumed magmatic arcs. Geology 38, 1071–1074.

Qian, J.H., Yin, C.Q., Wei, C.J., Zhang, J., 2019. Two phases of Paleoproterozoicmetamorphismin the Zhujiafang ductile shear zone of the Hengshan Complex: Insights into the tectonic evolution of the North China Craton. Lithos 330–331, 35–54.

Qian, J.H., Yin, C.Q., Zhang, J., Ma, L., Wang, L.J., 2018. High-pressure granulites in the Fuping Complex of the central North China Craton: metamorphic P-T-t evolution and tectonic implications. J. Asian Earth Sci. 154, 255–270.

Ren, L.D., Geng, Y.S., Du, L.L., Wang, Y.B., Guo, J.J., 2013. SHRIMP data on zircons from the Wanzi series: Constraints on the rock formation time and implications of migmatization at 2.1–2.0 Ga in the Fuping Complex, North China Craton. J. Asian Earth Sci. 72, 203–215.

Rogers, J.J.W., Santosh, M., 2002. Configuration of Columbia, a Mesoproterozoic Supercontinent. Gondwana Res. 5, 5–22.

Spear, F.S., 1993. Metamorphic phase equilibria and pressure-temperature-time paths. Mineralogical Society of America, pp 8.

Spear, F.S., Ashley, K.T., Webb, L.E., Thomas, J.B., 2012. Ti diffusion in quartz inclusions: implications for metamorphic time scales. Contrib. Miner. Petrol. 164, 977–986.

Spear, F.S., Wark, D.A., 2009. Cathodoluminescence imaging and titanium thermometry in metamorphic quartz. J. Metamorph. Geol. 27, 187–205.

Sun, Z.L., Li, J.R., Liu, C.R., Zhang, Y.S., Yang, Y.H., Yan, W.S., 2004. Another view on the Longquanguan Ductile shear zone. Geol. Survey Res. 27, 92–100 (in Chinese with English abstract).

Stipp, M., Stunitz, H., Heilbronner, R., Schmid, S.M., 2002. The eastern Tonale fault zone: a 'natural laboratory' for crystal plastic deformation of quartz over a temperature range from 250 to 700 °C. J. Struct. Geol. 24, 1861–1884.

Thomas, J.B., Watson, E.B., Spear, F.S., Shemella, P.T., Nayak, S.K., Lanzirotti, A., 2010. TitaniQ under pressure: the effect of pressure and temperature on the solubility of Ti in quartz. Contrib. Miner. Petrol. 160, 743–759.

Thomas, J.B., Watson, E.B., Spear, F.S., Wark, D.A., 2015. TitaniQ recrystallized: experimental confirmation of the original Ti-in-quartz calibrations. Contrib. Miner. Petrol. 169, 27.

Tullis, J., 1977. Preferred orientation of quartz produced by slip during plane strain. Tectonophysics 39, 87–102.

Tullis, J., Christie, J.M., Griggs, D.T., 1973. Microstructures and preferred orientations of experimentally deformed quartzites. Geol. Soc. Am. Bull. 84, 297–314.

Tullis, J., Yund, R.A., 1987. Transition fro cataclastic flow to dislocation creep of feldspar: mechanisms and microstructures. Geology 15, 606–609.

Vauchez, A., Tommasi, A., Mainprice, D., 2012. Faults (shear zones) in the Earth's mantle. Tectonophysics 558, 1–27.

Wan, B., Windley, B.F., Xiao, W., Feng, J., Zhang, J.e., 2015. Paleoproterozoic high-pressure metamorphism in the northern North China Craton and implications for the Nuna supercontinent. Nat. Commun. 6, 8344.

Wan, B., Yang, X.S., Tian, X.B., Yuan, H.Y., Kirscher, U., Mitchell, R.N., 2020. Seismological evidence for the earliest global subduction network at 2 Ga age. Science. Advances 6, eabc5491.

Wang, J., Kusky, T., Wang, L., Polat, A., Deng, H., 2015. A Neoarchean subduction polarity reversal event in the North China Craton. Lithos 220–223, 133–146.

Wang, J., Li, X., Ning, W., Kusky, T.M., Wang, L., Polat, A., Deng, H., 2019a. Geology of a Neoarchean suture: evidence from the Zunhua ophiolitic melange of the Eastern Hebei Province, North China Craton. Geol. Soc. Am. Bull. 131, 1943–1964.

Wang, M., Qian, J.H., Zhang, J.J., Zhang, B., 2019b. Zircon U-Pb age and Lu-Hf isotope characteristics of the granitic augen gneiss from the Longquanguan shear zone, and their geological significance. Earth Sci. Front. 26, 171–182 (in Chinese with English abstract).

Wang, Y.S., Zhu, G., Wang, D.X., Song, C.Z., 2005. An attempt to apply three geothermometers in the interpretation of low-temperature mylonites in the southern segment of the Tanlu fault zone. 32, 625–633.

Wark, D.A., Hildreth, W., Spear, F.S., Cherniak, D.J., Watson, E.B., 2007. Pre-eruption recharge of the Bishop magma system. Geology 35, 235–238.

Wark, D.A., Watson, E.B., 2006. TitaniQ: a titanium-in-quartz geothermometer. Contrib. Miner. Petrol. 152, 743–754.

Whitney, D.L., Evans, B.W., 2010. Abbreviations for names of rock-forming minerals. Am. Mineral. 95, 185–187.

Xia, H., Platt, J.P., 2019. Is the Vincent fault in southern California the Laramide subduction zone megathrust? Geol. Soc. Am. Bull. 131, 120–136.

Xia, X.P., Sun, M., Zhao, G.C., Wu, F.Y., Xu, P., Zhang, J., He, Y.H., Zhang, J.H., 2006. U-Pb age and Hf isotope study of detrital zircons from the Wanzi supracrustals: Constraints on the tectonic setting and evolution of the Fuping Complex, Trans-North China Orogen. Acta Geologica Sinica-English Edition 80, 844–863.

Xu, R.H., Zhu, M., Chen, F.K., Guo, J.H., 1995. A geochronological study of the Longquanguan ductile shear zone. Quaternary Sci. 332–342 (in Chinese with English abstract).

Zhang, H.C.G., Wang, J., Peng, T., Pham, V.T., Chen, Y.C., Hou, Q.L., Wu, C.M., 2018. Temperature conditions of mylonitization of the Dashuiyu ductile shear zone. Acta Petrol. Sinica 34, 1801–1812 (in Chinese with English abstract).

Zhao, G.C., Cawood, P.A., Wilde, S.A., Sun, M., 2002a. Review of global 2.1–1.8 Ga orogens: implications for a pre-Rodinia supercontinent. Earth Sci. Rev. 59, 125–162.

Zhao, G.C., Sun, M., Wilde, S.A., Li, S.Z., 2005. Late Archean to Paleoproterozoic evolution of the North China Craton: key issues revisited. Precambr. Res. 136, 177–202.

Zhao, G.C., Wilde, S.A., Cawood, P.A., Lu, L.Z., 1998. Thermal evolution of Archean basement rocks from the eastern part of the North China carton and its bearing on tectonic setting. Int. Geol. Rev. 40, 706–721.

Zhao, G.C., Wilde, S.A., Cawood, P.A., Lu, L.Z., 2000. Petrology and P-T path of the Fuping mafic granulites: implications for tectonic evolution of the central zone of the North China craton. J. Metamorph. Geol. 18, 375–391.

Zhao, G.C., Wilde, S.A., Cawood, P.A., Sun, M., 2001. Archean blocks and their boundaries in the North China Craton: lithological, geochemical, structural and P-T path constraints and tectonic evolution. Precambr. Res. 107, 45–73.

Zhao, G.C., Wilde, S.A., Cawood, P.A., Sun, M., 2002b. SHRIMP U-Pb zircon ages of the Fuping Complex: implications for late Archean to Paleoproterozoic accretion and assembly of the North China Craton. Am. J. Sci. 302, 191–226.

Zhao, L., Zhang, J.J., Liu, S.W., 2006. Syn-deformational granites of the Longquanguan ductile shear zone and their monazite electronic microprobe dating. Acta Petrol. Mineral. 25, 210–218 (in Chinese with English abstract).

Zhao, Y.F., Hu, J.M., Gong, W.B., Chen, H., 2019. Tectonic framework and deformation events in the central Trans-North China Tectonic Belt during the Late Paleoproterozoic. Earth Sci. Front. 26, 104–119.